L. S. Langston

Associate Professor,
Mechanical Engineering Department,
University of Connecticut,
Storrs, Conn.
Mem. ASME

Crossflows in a Turbine Cascade Passage

Measurements of the subsonic flow in a large scale plane turbine cascade, that were given in an earlier paper, are examined in more detail from the standpoint of the endwall boundary layer. Representative data are presented in terms of normal and streamwise velocities, flow angle deviations, and polar plots, that can be used to substantiate analytical models of the endwall flow. The qualitative behavior of the endwall crossflow was found to be correlated by a relatively simple expression, based on the flow angle deviation.

Introduction

An important problem that arises in the design of modern gas turbines and in the analysis of their performance, is the understanding and prediction of the nature and influence of secondary flows. Based on the current state-of-the-art, a turbine designer might well define secondary flows as those three-dimensional flow effects in a turbine that he had not planned on. One of the simplest of geometries in which to study these three-dimensional effects is a plane cascade of turbine airfoils.

Background. In an earlier paper, Langston, Nice, and Hooper [1] gave an experimental description of the secondary or three-dimensional flow in a large scale, low aspect ratio plane cascade of turbine airfoils. In their work, detailed measurements of subsonic flow were made at axial planes in front of, within and behind the cascade. The three-dimensional flow that they measured is shown schematically in Fig. 1. This figure shows that at the endwall of the cascade, the inlet boundary layer separates and forms a horseshoe (or leading edge) vortex, with one leg of the vortex in one airfoil passage and the other leg in the adjacent passage.

One leg merges with and becomes part of the *passage vortex*. Thus in a cascade flow, that part of the secondary flow that is called the passage vortex (a term first used by Herzig, et al. [2]) is an amalgamation of one leg of the horseshoe vortex (and hence part of the inlet boundary layer), the crossflow from the endwall boundary layer formed within the cascade, and entrained fluid from the mainstream flow in the cascade passage.

As shown in Fig. 1, the other leg of the horseshoe vortex which has been labeled the *counter vortex* remains in the suction surface-endwall corner. The counter vortex has a sense of rotation opposite to the passage vortex. It is much smaller than the passage vortex and may be dissipated by viscosity.

The ribbon arrow representation of both vortices in Fig. 1 has been drawn to exaggerate the vortex rotation, in order that the sense of rotation of each vortex would be clearly shown. The core of the passage vortex studied in reference [1] approximated a Rankine vortex. A particle of fluid that was near the viscous-inviscid interface of the Rankin vortex would actually have a total gross rotation of one or two revolutions about the center line of the passage vortex, as it passed through the cascade passage.

Crossflow Approach. While reference [1] gave an overall picture of the flow in a turbine cascade, it is the purpose of this paper to examine the data in greater detail, in terms of a three-dimensional crossflow boundary layer approach. The three-dimensional boundary layer referred to here is on the cascade endwall, inside the cascade passage. Regions of the endwall flow that are near singular points or separation and attachment lines are excluded from consideration. Also, the term *boundary layer* is used here in the spirit of the bounded boundary layer defined by Horlock [3], that is, endwall effects can be of the order of magnitude of the passage dimensions. It will be shown that it was not possible to use Horlock's concept exactly.

A bit of three-dimensional boundary layer history is in order at this point. Investigators have found that a convenient way to represent a three-dimensional boundary is to project the velocity profile onto two mutually perpendicular planes, one in a nominal free stream streamwise direction and one normal to the free stream streamwise direction. The latter is called the crossflow component.

Early on it was found that for small crossflows, the streamwise component of a three-dimensional boundary layer could be fairly

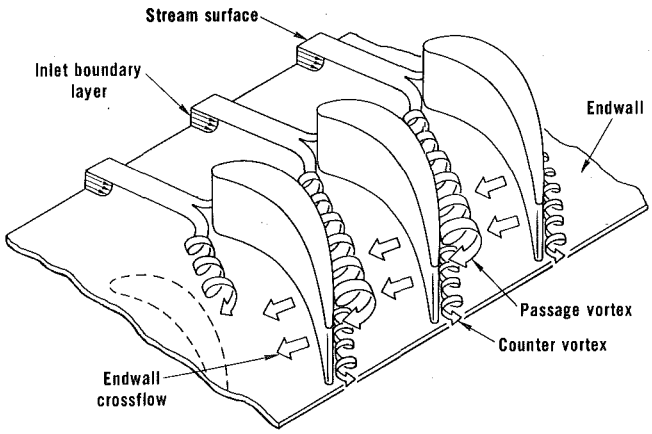

Fig. 1 The three-dimensional separation of a boundary layer entering a turbine cascade. The saddle point occurs where the vortex is formed

Contributed by the Gas Turbine Division and presented at the Gas Turbine Conference and Products Show, New Orleans, La., March 10–13, 1980, of THE AMERICAN SOCIETY OF MECHANICAL ENGINEERS. Manuscript received at ASME Headquarters, December 3, 1979. Paper No. 80-GT-5.

accurately represented by an equivalent two-dimensional boundary layer, with a velocity profile of the form

$$\frac{u_s}{u_{s_{ms}}} = \left(\frac{z}{\delta}\right)^{1/n} \tag{1}$$

where n is a specified constant.

The problem of predicting the crossflow component was treated by using a polar plot of the two velocity components, i.e., a plot of the crossflow velocity component versus the streamwise component. This plot in effect places an imaginary observer atop the velocity profile, watching the loci of the tips of the velocity vectors in the boundary layer below him.

Johnston [4] was one of the first to use the polar plot, and a typical Johnston triangular polar plot is shown in Fig. 2(*a*). It is given by the expression

$$\left.\begin{aligned} \frac{u_n}{u_{s_{ms}}} &= \frac{u_s}{u_{s_{ms}}} \tan \epsilon_w, \qquad z < z^+ \\ \frac{u_n}{u_{s_{ms}}} &= \left(1 - \frac{u_s}{u_{s_{ms}}}\right) \tan \alpha, \qquad z > z^+ \end{aligned}\right\} \tag{2}$$

where u_n, u_s and $u_{s_{ms}}$ are the crossflow, streamwise, and free stream velocities, respectively. The region $z > z^+$ usually accounts for 95 to 99 percent of the boundary layer. Given values of z^+ and α, equation (2) has been shown many times to be a good representation of small crossflows on flat plate geometries. Other small crossflow models are discussed by Nash and Patel [5].

An example of another type of crossflow polar plot is shown in Fig. 2(*b*). This is called a crossover, crossflow plot and can represent crossflow in a flow that earlier in its history had been skewed in the opposite direction, so that u_n changes sign. Klinksiek and Pierce [6] observed this type of flow on the endwall of the second bend in an S-shaped duct. Both Shanebrook [7] and Eichelbrenner [8] have proposed various polynomial expressions to describe the crossover, crossflow polar plot. One form given by Eichelbrenner is a polynomial of the form,

$$\frac{u_n}{u_{s_{ms}}} = \frac{u_s}{u_{s_{ms}}} \tan \epsilon_w \left\{1 + c_1\left(\frac{u_s}{u_{s_{ms}}}\right) + c_2\left(\frac{u_s}{u_{s_{ms}}}\right)^2 + \ldots\right\} \tag{3}$$

where $c_1, c_2, \ldots$ are evaluated from boundary conditions at the edge of the boundary layer and at the wall. Almost any kind of crossflow can be described by equation (3), provided that enough terms in the polynomial are used.

During the 1960's a good deal of work was done in an attempt to find "the best" representation of a general polar plot that would apply to a wide range of three-dimensional boundary layers. Two conclusions came out of this work:

1 In a summary of this work, Johnston [9] concluded that there is no general universal crossflow profile. The flow in three-dimensional boundary layers is dependent in each case on boundary conditions and flow history.

2 As Wheeler and Johnston [10] have pointed out, without a so-called universal crossflow profile, three-dimensional prediction methods using integral techniques cannot be general enough to work on a variety of geometric configurations.

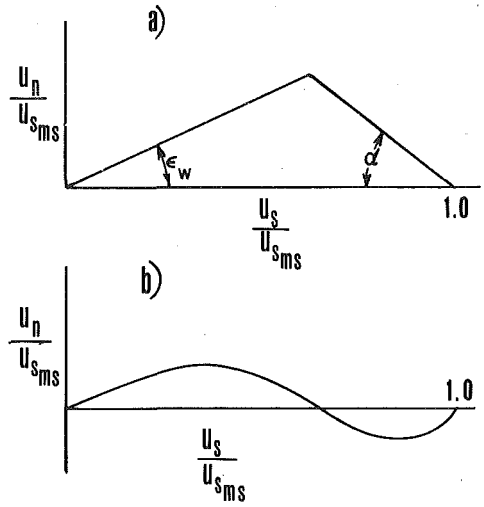

Fig. 2 Polar plots. (*a*) Johnston triangular; (*b*) crossover, crossflow

This then has led to an abandonment of integral methods in favor of methods that use finite difference approximations to the differential boundary layer equations. Examples of this latter approach are the work of Pratap and Spalding [11], Briley and McDonald [12], Dodge [13], and Ghia, et al. [14].

However, the crossflow boundary layer approach and the polar plot still provide a useful and simple picture of a three-dimensional boundary layer which is not conveyed by other representations. It is a convenient way of categorizing or "botanizing" a three-dimensional flow. It is very difficult to represent truly three-dimension flows, which if described through experimental results, may mean several thousand data points (as in the case of reference [1]), or if predicted, may mean many pages of computer printout. The polar plot provides a simple way of summarizing these results.

Objectives. It is the purpose of this paper to present the crossflow characteristics of the endwall boundary layer of a plane turbine cascade. Based on a correlation of the flow angle deviation data, a new empirical crossflow model for endwall flow in a turbine cascade is presented.

This presentation is important for the following reasons:

1 As far as the author is aware of, there are no data available in the open literature that give a complete picture of the turbine cascade endwall boundary layer in a crossflow boundary layer format. Waterman and Tall [15] showed measurements of total pressure in the throat and exit plane of turbine nozzle cascades, but gave no velocity measurements. Sjolander [16] took velocity measurements in a passage of a low-turning inlet guide vane annular cascade. However, all

Nomenclature

a = constant in equation (5)
b_x = axial chord
c = constant in polynomial polar plot
c_{p_t} = total pressure coefficient, $(P_{to} - P_t)/{}^1/_2\rho_0 U_0^2$
n = exponent in equation (1)
P = pressure
u = velocity
U_0 = upstream inlet velocity to cascade
u_n = crossflow velocity
u_s = streamwise velocity
x = coordinate normal to cascade leading edge, nondimensionalized on b_x
y = coordinate parallel to cascade leading edge, nondimensionalized on b_x
z = coordinate prependicular to endwall, nondimensionalized on b_x
z_0 = value of z where $\epsilon = 0$
z_1 = values of z where ϵ is a minimum
z^+ = apex coordinate of Johnston triangle polar plot
α = angle of inviscid portion of Johnston triangle polar plot
β_1 = airfoil mean camber line inlet angle, measured from y axis
β_2 = airfoil mean camber line exit angle, measured from y axis
γ = constant in equation (5)
δ = boundary layer thickness
ϵ = yaw angle deviation, $\theta - \theta_{ms}$
θ = yaw angle
ρ = density
ϕ = pitch angle

Subscripts

ms = midspan or free stream
t = total
x = component in x-direction
w = wall
0 = upstream
1, 2 = indices

of his measurements were taken using a cobra probe, with no provision made for pitch angle variation in the flow. Carrick [17] took extensive measurements inside a low-turning plane cascade passage, but did not report his results in a way that one could make a quantitative assessment of the crossflow in the endwall boundary layer. Marchal and Sieverding [18] took detailed velocity measurements in both a nozzle and a rotor plane cascade. They showed secondary velocities and area-averaged flow angles, but they did not give complete velocity data.

2 The crossflow characteristics to be presented are based on a survey of the entire flow field of a cascade passage. This is very important, especially in internal flows. Wrong conclusions can be drawn if only a few traverses are made in a passage.

3 There is more and more evidence that the endwall flow shown in Fig. 1 is a very general picture of turbine cascade endwall flows for a wide range of cascade geometries and inlet conditions. Sjolander [16] found a similar endwall flow at the i.d. of an annual cascade. Marchal and Sieverding [18] report the same flow picture for both a nozzle (with two different inlet boundary layers) and a rotor cascade. Carrick [17] got the same qualitative endwall flow, even for cases of high inlet boundary layer skew produced by a moving belt at the inlet of his cascade. The author has observed soot and ceramic coating discoloration patterns in the nozzles of turbines in aircraft jet engines after many hours of operation, that suggest the same flow picture.

Thus a case can be made here that, because of the strong favorable pressure gradients in turbine cascades, the endwall boundary layer flow is qualitatively the same over a wide range of conditions. Hence any crossflow models and polar plots based on cascade data can in turn be expected to be quite general.

Experimental Apparatus

Testing was conducted in a large-scale, low-speed cascade wind tunnel that is described in more detail in reference [1]. Measurements were taken at various axial locations through one of the cascade passages, using conventional instrumentation that will be described in the following. The cascade geometry is as follows:

Axial chord, b_x = 11.08 in. (0.2813 m)
Chord/axial chord = 1.2242
Pitch/axial chord = 0.9555
Aspect ratio (span/axial chord) = 0.9888
Airfoil mean camber line angles
β_1 = 43.99 deg
β_2 = 25.98 deg

The airfoil sections, cascade coordinate system and measurement plane positions are shown in Fig. 3. All lengths shown are normalized on the axial chord, b_x. As illustrated in Fig. 3, $x = 0$ is at the leading edge plane and $y = 0$ is at the trailing edge plane tangency point on airfoil 2. The coordinate $z = 0$ is in the endwall plane, with the z axis positive into the flow. Also shown is the yaw angle, θ, measured in xy planes from the x-axis. The pitch angle of the flow, ϕ, defined as the angle between an xy plane and the local velocity vector, is taken as positive away from the endwall.

Most of the flow field in the cascade was mapped by using a five-hole probe that enabled the measurement of total pressure, static pressure, and velocity direction in the flow field, to within 0.1 in. (0.25 cm) of the endwall. Details of the probe are given in reference [1].

Flow velocities near the endwall were measured using both a single sensor hot wire probe and single sensor hot film probe. The data, used here, will deal only with measurements taken with the hot film probe. These were made with a Thermo-Systems Model 1210-20 hot film probe that had a cylindrical sensor with a diameter of 0.002 in. (0.05 mm) and a length of 0.040 in. (1.0 mm). The hot film was located off the wall by noting when electrical contact occurred between a downstream probe foot and a thin, very smooth layer of aluminum foil that covered the entire endwall for the hot film tests. Hot film positioning normal to the endwall was done with a micrometer drive. Flow measurements were taken 0.02 cm (0.008 in.) from the wall as measured from the hot film cylindrical sensor center line, to a sufficient distance away from the endwall so that hot film and five-hole probe data overlapped.

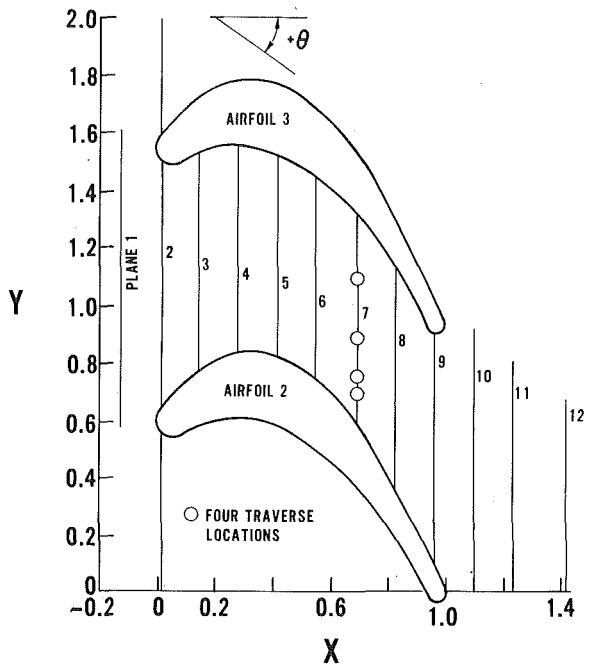

Fig. 3 Airfoil section and *xy* coordinate system. The *z* coordinate is positive into the plane of the page

Test Conditions

All tests were run with the cascade set at an inlet air angle of 44.7 deg. The upstream inlet velocity, U_0, was 110 ft/s (33.5 m/s) corresponding to inlet and exit Reynolds numbers based on blade axial chord of 5.9×10^5 and 10×10^5, respectively.

The characteristics of the equilibrium boundary layer entering the cascade were measured at a point upstream of the cascade (see reference [1]) and were found to have the following values:

Boundary layer thickness	1.3 in. (3.30 cm)
Displacement thickness	0.148 (0.376 cm)
Momentum thickness	0.110 (0.279 cm)
Shape factor	1.35
Momentum thickness Reynolds number	5338

The values for displacement thickness, momentum thickness, and momentum thickness Reynolds number are slightly different from those given in reference [1], due to an error found after the publication of the latter.

Experimental Results

The purpose here is to show the general characteristics of the endwall flow downstream of the endwall saddle point and its separation lines, and unstream of the cascade passage trailing edges. This excludes about 5–10 percent of the passage endwall area. In this way the complexities of the three-dimensional flow separations occurring at or near these locations are avoided, so that the details of a major part of the endwall flow can be treated with an added degree of simplicity.

Because of the large amount of data taken, only the results of flow measurements taken in plane 7 at an axial position of $x = 0.69$ (see Fig. 3) will be presented. Four selected spanwise traverses taken from the endwall to midspan at the gapwise positions of $y = 0.692$, 0.766, 0.903, and 1.106, all in plane 7, will be examined in detail to illustrate crossflow characteristics. Since the entire flow field in front of the passage, at eight planes within the passage and at three planes downstream of the passage, was surveyed, it can be stated with confidence that plane 7 data are representative of the endwall boundary layer. Again the purpose here is to present the dominant streamwise and crossflow features of the endwall boundary layer.

Flow Field Measurements. The distribution of total loss in plane 7 is shown in Fig. 4, as an isobar plot of the total loss coefficient, c_{p_t}. In this plane the observer is looking upstream, into the flow. The passage vortex is evidenced by the closed isobars or Bernoulli surfaces, near the suction surface side of the passage. As shown by the plot, the viscous region of endwall boundary layer is very thin. High losses appear on the endwall near the suction side corner where the endwall boundary layer separates from the endwall (at about $y = 0.7$) and where the suction surface boundary layer separates from the airfoil (at about $z = 0.23$). Also shown in Fig. 4 are the locations of the four spanwise traverses that will be examined in detail. These were chosen out of the total of 14 traverses that were made in plane 7, to show the characteristics of the endwall flow, (a) near the pressure surface, (b) near the inviscid-viscous region of the passage vortex, (c) at the pressure-side of the passage vortex core, and (d) at the suction-side of the passage vortex core.

Figure 5 is a plot of some of the velocity vector components in plane 7, showing the details of the secondary flow in the suction side of the passage. This plot was obtained by calculating the in-plane components of the measured velocity and for each spanwise probe traverse, vectorially subtracting the midspan component from the in-plane velocities of that traverse. Since the midspan static pressure distribution was shown in reference [1] to agree well with a two-dimensional potential flow calculation, the velocity vectors in Fig. 5 also show the deviation from potential flow.

One can see the motion of the passage vortex in Fig. 5, with its center of rotation at approximately $y = 0.73$, $z = 0.1$. This closely coincides with the center of the closed Bernoulli surfaces in Fig. 4, and, although not shown here, with the location of lowest static pressure measured in the plane. To delinate the viscous and inviscid parts of the vortex, the isobar $c_{p_t} = 0.1$ from Fig. 4 has been replotted in Fig. 5. It can be seen from the velocity vectors and the isobar that the passage vortex in plane 7 has the features of a distorted Rankine vortex. Part of this distortion is due to the fact that plane 7 is not a Trefftz plane. Also shown in Fig. 5 are the locations of three of the four traverses that will be treated below.

Velocity Profiles. Figure 6 shows a plot of the normal and streamwise velocity distributions at each of the four selected traverses in plane 7. Normal velocities are taken as positive towards the suction side. The data shown closest to the wall for values less than $z = 0.01$, are taken from the hot film measurements. For each spanwise traverse shown in Fig. 6, the free stream velocity magnitude and direction is taken as the midspan velocity, $u_{s_{ms}}$. The values of the midspan velocities and their associated yaw angles are listed in Table 1, so that the normalized velocities in Fig. 6 can be converted and compared in absolute values to one another.

As shown by the secondary flow velocity vectors in Fig. 5, the crossflow is smallest in the pressure side of the passage, and this is also shown in Fig. 6(a) for a position close to the pressure side. The crossflow profile in Fig. 6(a) is typical of small crossflows of the Johnston-triangular plot variety discussed in the introduction. The streamwise profile shown in Fig. 6(a) shows a decrease in velocity at about $z = 0.04$. However, this is not a true indication of a boundary layer thickness, since no change in total pressure was measured, even for the closest 5-hole probe position at $z = 0.01$. This was true for much of the endwall on the pressure side of the passage, i.e., that the viscous boundary layer was very thin.

Both of the crossflow profiles in Figs. 6(b) and 6(c) exhibit the presence of the passage vortex, and each show a crossover crossflow profile, i.e., in addition to the endwall crossflow toward the suction side, there is a return flow toward the pressure side. These have the same shape as some of the crossover, crossflow profiles measured by Klinksiek and Pierce [6], mentioned earlier.

When the streamwise velocity profiles in Figs. 6(a) and 6(b) are compared, one is tempted to say that there is a thickening of the endwall boundary layer as the suction side is approached, since u_s seems to show conventional boundary layer behavior at about $z = 0.08$ in Fig. 6(b) as opposed to $z = 0.04$ in Fig. 6(a). However, it would be incorrect to use two-dimensional boundary layer concepts for the data shown in Fig. 6(b). The total pressure-results at this gapwise position

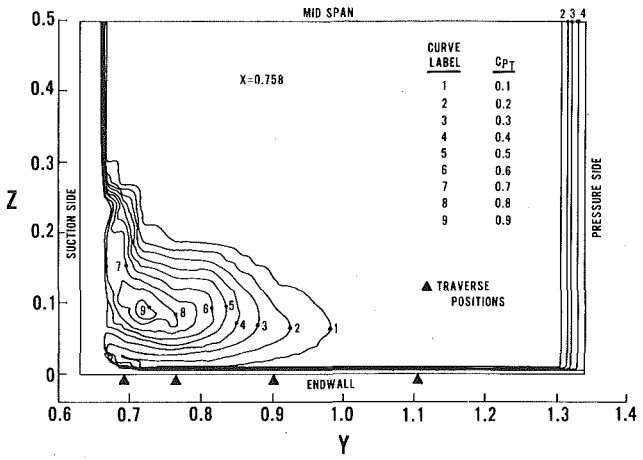

Fig. 4 Isobar plot of total pressure loss coefficients in plane 7. Four traverse positions are indicated

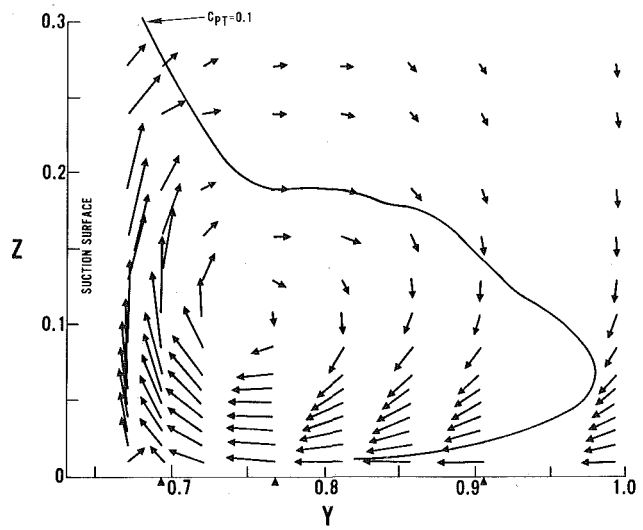

Fig. 5 Secondary flow velocity vectors in plane 7, near suction side. Loss contour $c_{p_t} = 0.1$ is shown for the passage vortex.

(see Fig. 4) show that total pressure is not a monotonic function of distance away from the wall, due to the passage vortex. The streamwise velocity profiles in Fig. 6(c) also clearly shows the effect of the passage vortex and certainly could not be modeled by a two-dimensional equilibrium boundary layer profile, such as given by equation (1).

The velocity profiles that are typical of the region in the suction side of the passage vortex core are shown in Fig. 6(d). No hot film data were taken at this position because of their proximity to the passage vortex separation line in the suction side-endwall corner. In this region the flow near the endwall had high pitch angles, and, since the hot film could only be traversed in a spanwise direction, hot film measurements would have been inaccurate. Again, the streamwise profile is far from a two-dimensional flow. When compared to Figs. 6(b) and 6(c) the crossflow profile on the suction side of the vortex shows smaller positive crossflows, as the endwall flow approaches separation.

The data presented in Fig. 6 represent measurements of the mean flow field only. As was stated in reference [1], turbulence intensity measurements were taken, but due to the extreme thinness of the endwall boundary layer, it was not possible to ascertain its state, i.e., whether it was laminar or turbulent. All that could be said was that there was a rise in turbulence intensity as the wall was approached. Also, any hot film or hot wire measurements made near a separation line or near the core of the passage vortex showed a sharp rise in intensity values over free stream values.

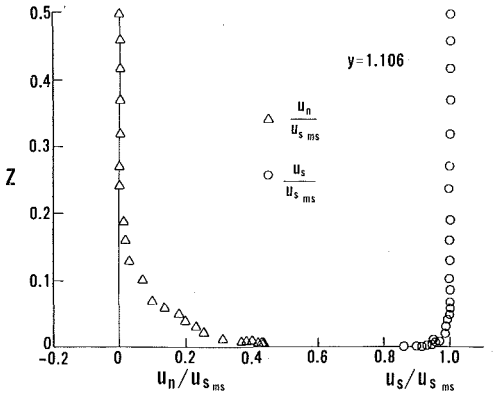

Fig. 6 (*a*)

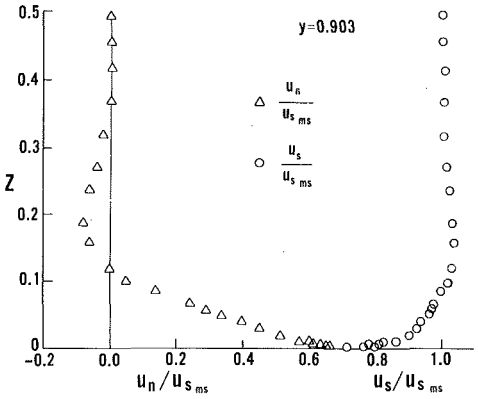

Fig. 6 (*b*)

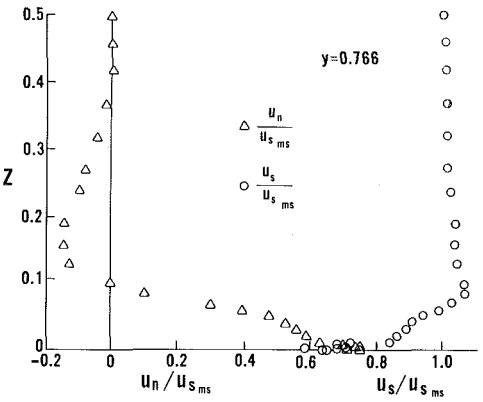

Fig. 6 (*c*)

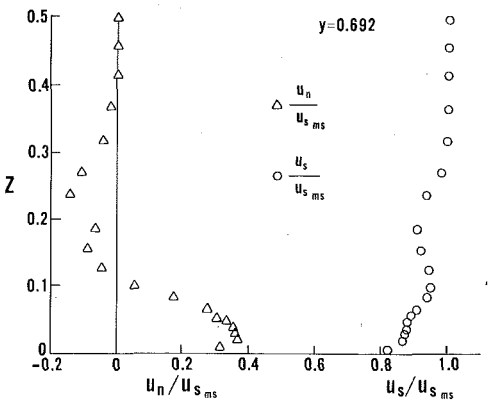

Fig. 6 (*d*)

Fig. 6 Streamwise and crossflow velocities in plane 7 at four traverse locations, as a function distance from the endwall

Yaw Angle Deviation. The yaw angle deviation, ϵ, is an important variable in three-dimensional boundary layers, because ϵ determines the relationship between the streamwise velocity and the normal velocity, i.e.,

$$\frac{u_n}{u_s} = \tan \epsilon. \tag{4}$$

The yaw angle deviation for each of the four traverses in plane 7 is shown in Fig. 7 as a function of normalized distance from the endwall, z. The absolute yaw angles can be calculated from these plots by using the midspan absolute yaw angles listed in Table 1. The angles were measured with the five-hole probe nulled in yaw, and with the hot film by noting the yaw angle at which velocity was a maximum. Positive values of ϵ represent flow towards the suction side of the passage.

The limiting streamline or wall angles shown at $z = 0$ in Fig. 7 were calculated by carefully extrapolating the hot film angle measurements to $z = 0$, on a separate, large-scale plot. The possible underprediction of the limiting streamline angle by using this extrapolation method has been pointed out by Johnston [9]. However it was felt that this method was adequate for the present study for the following reasons:

1 Considering the scale of the channel, hot film measurements were taken very close to the endwall, to within 0.02 cm (0.008 in.), closer than the case that Johnston cited to prove his point.

2 Endwall flow visualization measurements were made using ink injected onto the endwall (see reference [1]). However it was felt that ink traces tended to give lower values of ϵ, whenever the skew was high, due to higher inertia forces on the ink droplet. Values of wall angles measured from the ink traces are given in Table 1, and it can be seen that they are lower than those obtained by extrapolation.

Figure 7(*a*) shows the yaw angle deviation for $y = 1.106$, the position nearest the pressure side, where the crossflow is small. Figures 7(*b*) and 7(*c*) show the deviation for positions closer to and to the right of the passage vortex center line. Both show a typical crossover crossflow behavior. The yaw angle deviation for the position to the left of the passage vortex center line in Fig. 7(*d*) shows a similar behavior, except that near the wall, the values of ϵ start to decrease, possibly because of its close proximity to the suction side endwall separation line. No wall value was calculated for Fig. 7(*d*) since no hot film data were taken at this position because of the high pitch angles.

The yaw angle deviations shown in Fig. 7 are representative of the endwall flow in the passage. An examination of all of the yaw angle deviation data showed that the *qualitative* behavior of the yaw angle deviation could be correlated by a single equation,

$$\epsilon = (\epsilon_w - az)e^{-\gamma z} \tag{5}$$

where ϵ_w—wall value of ϵ

a—crossover crossflow coefficient

γ—crossflow strength coefficient

z—nondimensional distance from the endwall

Also, ϵ is defined in the interval $-\pi/2 < \epsilon < \pi/2$, since values outside of this interval would signify three-dimensional separation.

Table 1 Midspan values and equation (5) constants for four traverses in plane 7, $x = 0.758$

y	0.692	0.766	0.903	1.106
$u_{s_{ms}}/U_0$	1.884	1.796	1.568	1.149
θ_{ms}	51.5°	47.0°	42.6°	42.9°
ϵ_w	—	60°	51°	33°
a	—	612°	405°	0
γ	—	16.13	15.63	19.49
$(\epsilon_w)_{\text{ink}}$	5°	45°	47°	26°

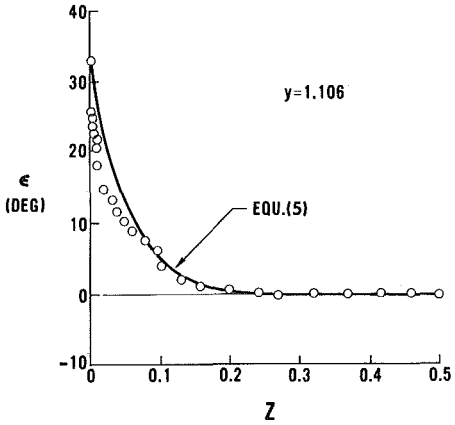

Fig. 7 (a)

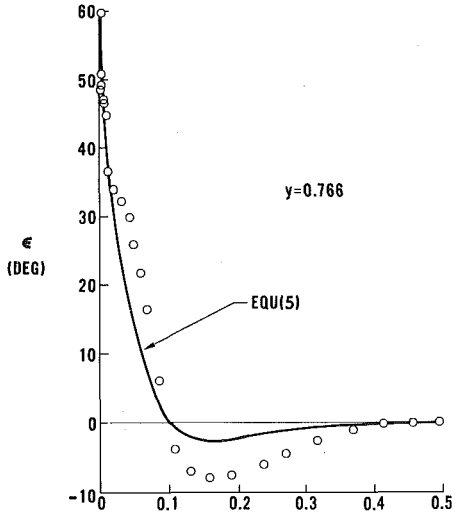

Fig. 7 (c)

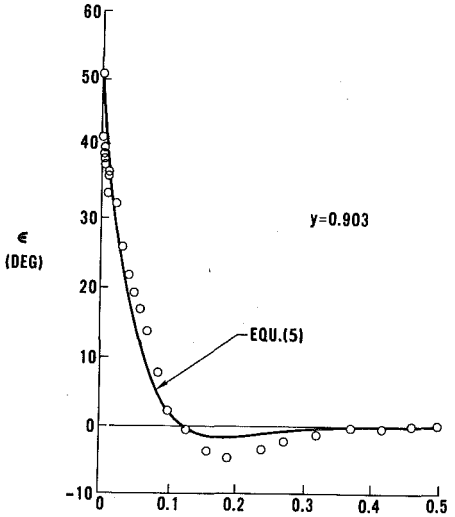

Fig. 7 (b)

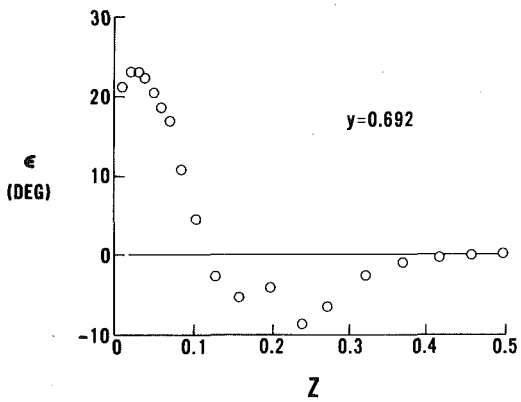

Fig. 7 (d)

Fig. 7 The yaw angle deviation as a function of distance from the endwall for four traverse locations in plane 7

Equation (5) is plotted in Figs. 7(*a*), 7(*b*) and 7(*c*). It is not plotted in Fig. 7(*d*) because it was found to be inadequate to describe regions of the flow that were near the separation line. The crossover, crossflow coefficient, a, was calculated from equation (5) at the point $\epsilon = 0$, or

$$a = \frac{\epsilon_w}{z_0} \tag{6}$$

where z_0 is the value of z where $\epsilon = 0$. In the case of Fig. 7(*a*) (the case of simple crossflow) this occurred essentially at $z \to \infty$, so that from (6), $a = 0$ for this case. For the case of Figs. 7(*b*) and 7(*c*), where there is a cross-over crossflow profile, the values are given in Table 1.

The crossflow strength coefficient was evaluated at the point where the data showed a minimum value of ϵ, i.e., where

$$\frac{d\epsilon}{dz} = 0 \text{ at } z = z_1. \tag{7}$$

The combination of equations (5) and (7) gives an expression for γ,

$$\gamma = \frac{a}{az_1 - \epsilon_w} \tag{8}$$

For the data shown in Fig. 7(*a*), where ϵ decreases monotonically with increasing z, γ was calculated by using equation (5) and the value given by the data at $z = 0.1$. Values of γ are listed in Table 1.

With three experimentally determined constants in equation (5), there are other ways that the data in Fig. 7 could have been fitted. As it is, equation (5) described the data in Figs. 7(*a*), 7(*b*) and 7(*c*) in a reasonably qualitative way. Taking the limit as z gets large in equation (5) and using L'Hospital's rule yields

$$\lim_{z \to \infty} \epsilon = 0 \tag{9}$$

This condition of zero crossflow at large values of z is seen to be in good agreement with the data at the midspan value of $z = 0.5$. One could also speculate that equation (5) might provide a better quantitaive fit of the data for the case of a higher aspect ratio passage, rather than the rather low aspect ratio passage of this study.

Equation (5) also yields a constantly turning velocity vector, right down to the wall; that is, from equation (5)

$$\left.\frac{d\epsilon}{dz}\right|_{z=0} = -(a + \gamma\epsilon_w), \tag{10}$$

which is what the data presented in Figs. 7(*a*), 7(*b*), and 7(*c*) seem to indicate.

Polar Plots. The polar plots that represent the endwall flow (except near regions of three-dimensional separation) in the passage are shown in Fig. 8. In this figure the data points have been connected by straight line segments to show the data point sequence. Thus the angle of the line connecting the origin and the nearest data point should not be interpreted as representing the wall angle, ϵ_w.

Figure 8(*a*) shows the polar plot for the transverse position near the pressure side of the passage. As was seen in Fig. 6(*a*), the crossflows are small in this region, and the plot in Fig. 8(*a*) exhibits a typical Johnston triangular polar plot type of behavior, given by equation (1).

The polar plots in Figs. 8(*b*), 8(*c*) and 8(*d*) exhibit crossover, crossflow behavior. In these regions closer to the suction side of the passage the flow is strongly affected by the passage vortex. All exhibit a "hooked" shape. This is characteristic of a traverse made through some part of a vortex, i.e., there is crossflow in both directions. Positive values on the polar plot indicate flow towards the suction side of the passage.

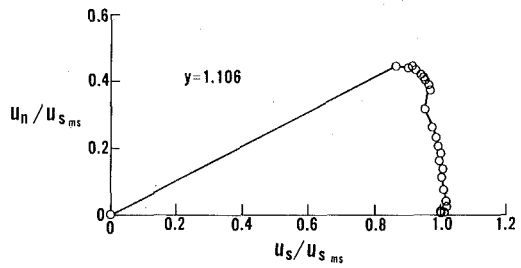

Fig. 8 (*a*)

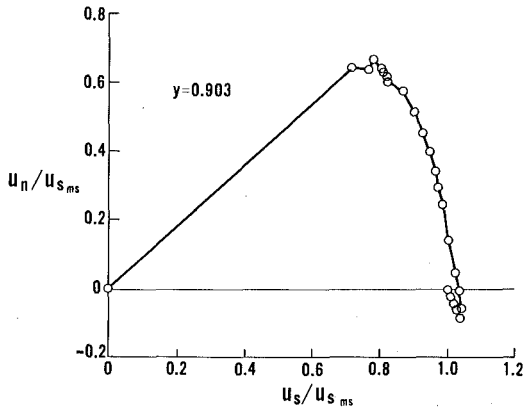

Fig. 8 (*b*)

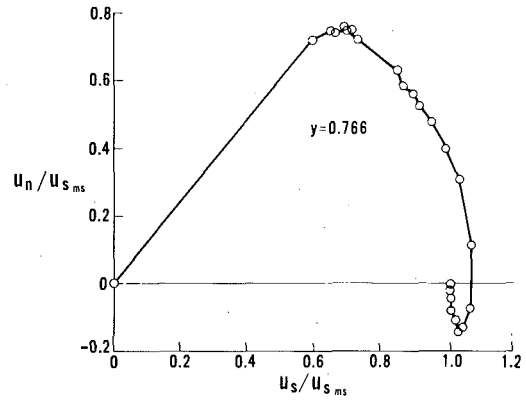

Fig. 8 (*c*)

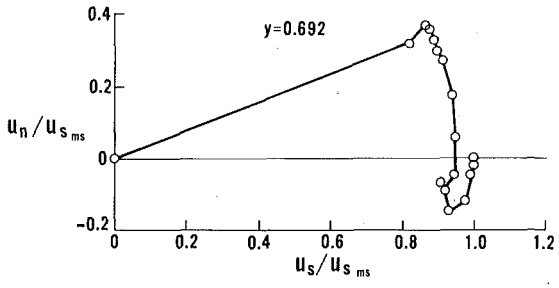

Fig. 8 (*d*)

Fig. 8 Polar velocity plots for four traverse locations in plane 7

Figures 8(*b*) and 8(*c*) show traverses made to the right of the vortex center and they both show a "backward hooked" behavior. That is, for each of these traverse positions, the flow represented by the hooked region is accelerated relative to the midspan velocity at that gap position. In both of these plots the hot film velocity values at the apex of the polar plot (i.e., the region of highest positive crossflow velocity) show that the viscous region of the endwall boundary layer is very close to the wall.

Figure 8(*d*) shows the polar plot for the traverse position close to the endwall separation line and to the left of the passage vortex center, as viewed in Fig. 5. As was stated earlier, no hot film data were taken at this position. This polar plot shows that flow has been decelerated relative to midspan. This type of behavior could be called a "forward hooked" polar plot.

Discussion

Combining equations (4) and (5) yields an expression for the crossflow in terms of the streamwise flow,

$$\frac{u_n}{u_s} = \tan[(\epsilon_w - az)e^{-\gamma z}] \tag{11}$$

This expression qualitatively describes the two types of polar plots found in this study of the endwall flow. These are shown in the sketch shown in Fig. 9.

For values of $a = 0$, $\epsilon_w \geq 0$ and $\gamma > 0$, Fig. 9(*a*) shows the Johnston-like polar plot that equation (11) would yield for crossflow near the pressure side of the passage, i.e., the region of small crossflow, furthest away from the influence of the passage vortex. For values of $a > 0$, $\epsilon_w > 0$ and $\gamma > 0$, equation (11) yields the crossover polar plots shown in Figs. 9(*b*) and 9(*c*), for the suction side of the passage, where the passage vortex is dominant. Figure 9(*b*) typifies the pressure side of the passage vortex, while Fig. 9(*c*) typifies the suction side of the vortex.

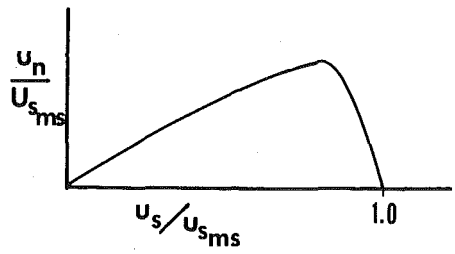

Fig. 9 (*a*)

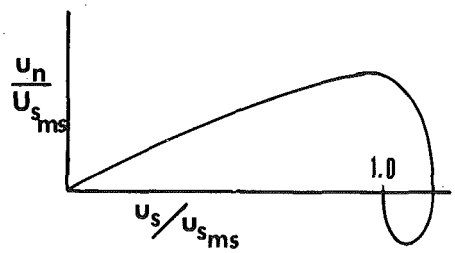

Fig. 9 (*b*)

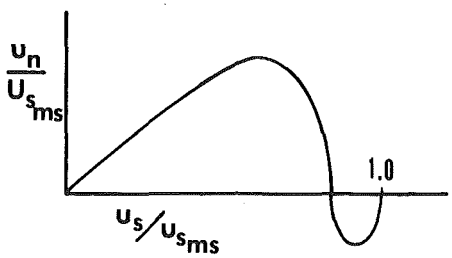

Fig. 9 (*c*)

Fig. 9 Polar plots for crossflow in a turbine cascade given by equation (11)

It should be stated here that equation (11) is simply a correlation of the crossflow data of this study. The range of the constants a, ϵ_w, and γ given in Table 1 is typical of the rest of the endwall data considered, and since equation (11) is a qualitative rather than a quantitative correlation of this very complicated, low aspect ratio endwall flow, there is no need to list additional values of these constants. Equation (11) has three experimentally determined constants, and, as such, is no more general than, say, a third-degree polynomial proposed by Eichelbrenner [8], given by equation (3). Also, as pointed out in the section on velocity profiles, no simple two-dimensional approximation could be made for u_s, the streamwise component of velocity, so that equation (11) cannot be used in a predictive fashion without knowledge of the spanwise variation of u_s.

However, equation (11) does qualitatively correlate the crossflow aspect of the endwall flow, something that Klinksiek and Pierce [6] were unable to do with the polar plot polynomial models of Shanebrook [7] and Eichelbrenner [8] (equation (3)) for their flow in an S-shaped duct. It is felt that this correlation of the endwall flow in a turbine passage is valuable, given that the endwall flow seems always to have the same character over a wide range of conditions, as was brought out in the introduction of this paper.

This correlation can provide a check of other data and analytical models of endwall flow. For instance, in one of the first attempts to do a turbine endwall boundary layer analysis, Dring [19] used an integral boundary layer approach. Booth [20] later extended this analysis to include the effects of compressibility and heat transfer. Both of these analyses used a small crossflow model, i.e., Fig. 9(a), with $a = 0$ in equation (11). The predicted losses that they reported were well below measured values. It is suggested here that one factor contributing to this discrepancy was caused by not using a crossflow model that included the case of $a > 0$. (Figs. 9(b) and 9(c)).

Another area in which equation (11) would be useful is in the evaluation of duct flows that are used to simulate flow in a turbine cascade. Because of the simpler geometry of a duct, it is frequently used for this purpose (see Barber and Langston [21]). For instance, the integral method models of Dring and Booth are duct flow models, as well as the more recent finite difference analyses of Briley and McDonald [12], and Dodge [13]. One of the most extensive experimental duct flow studies done to simulate flow in the turbine nozzle passage was carried out by Stanitz [22]. Had these investigators reported their data in a crossflow format (which they did not), the duct flow polar plots (and ranges of a, γ, and ϵ_w) could have been compared to those given here.

Some of the features of the endwall flow presented here are shared by the bounded boundary layer model proposed by Horlock [3]. By using the secondary flow model of Mellor and Wood [23], Horlock was able to derive gap-averaged expressions for the crossflow velocity in a turning passage. He was able to calculate a polar plot similar to that shown in Fig. 8(d) and to obtain a gap-averaged yaw angle deviation similar to Figs. 7(b) and 7(c).

No direct comparison could be made to his model because one of the key assumptions made was that the boundary layer thickness (defined as the point where total pressure begins to decrease) was of the same order as the passage width. This was not the case in the present study where, as has been shown, the actual endwall boundary layer (using Horlock's definition), was very much smaller than any passage dimension. Also, as he pointed out, the analysis was for small turning where the rotation of Bernoulli surfaces was not large, which was not the case for the data presented here. In addition, the cases that he calculated were for a large aspect ratio passage, while the present study is for a relatively low aspect ratio.

One other point that can be made here is the need for complete measurement surveys of a cascade passage or a duct when three-dimensional boundary layer measurements are made. In their measurements of the endwall boundary layer on the second bend of an S-shaped duct, Klinksiek and Pierce [6] obtained crossover, crossflow polar plots similar to Figs. 9(b), 8(b), and 8(c). The skewing that they reported was less than in the present study, but this is to be expected, since secondary flows in ducts are in general lower in magnitude than in a cascade of the same turning (see reference [21]). They explained their results using external flow boundary layer arguments to account for the phenomenon of flow reversal in the endwall boundary layer of the second duct, with simultaneous skewing occurring in two lateral directions. Their measurements were taken along the center line of the duct, only.

It is suggested here that what they observed in the second duct was actually the passage vortex of the first duct, and that, in internal flows, the occurrence of a crossover, crossflow profile signals the presence of a vortex. The flow visualization studies of Herzig, et al. [2] in tandem cascades support this view. Their work shows that the passage vortex of the upstream cascade passed through the downstream cascade (corresponding to the second bend of Klinksiek and Pierce) completely intact, and showed a high resistance to being turned by the second cascade. Had Klinksiek and Pierce taken more extensive measurements in their duct, this question might have been answered.

Summary and Conclusions

In this paper features of the endwall flow in a plane turbine cascade were examined in detail, using a crossflow boundary layer approach. Regions of the endwall that were near areas of three-dimensional separation were excluded. The following was concluded:

1 The endwall boundary layer region is characterized by small crossflows near the pressure side of the passage and large crossflows near the suction side. Extensive crossflows occur in inviscid parts of the flow and make the usual definition of a boundary layer difficult to apply. The actual portion of the flow that was effected by viscous forces near the endwall, was very thin and was characterized by the highest values of crossflow velocity and yaw angle deviation.

2 The crossflow data showed a Johnston triangular polar plot behavior near the pressure side and a crossover crossflow polar plot behavior in the suction side of the passage. The streamwise flow was found to be not similar to a two-dimensional boundary layer flow.

3 The qualitative behavior of the endwall crossflow was found to be correlated by a relatively simple expression (equation (11)). This expression for crossflow requires knowledge of the streamwise velocity, and three experimentally determined constants that specify the limiting streamline angle (ϵ_w), the relative crossflow strength (γ), and the extent of reverse crossflow (a). Ranges of these constants have been given.

One final conclusion of this paper is that further experimental work in high aspect ratio passages with smaller and simpler crossflows is needed, to evaluate how accurate the crossflow model presented is, in a quantitative sense.

Acknowledgments

The author wishes to express his gratitude to M. L. Nice for the many discussions that were held on this work and to R. M. Hooper for his spirited efforts in the experimental work. The experimental work reported here was supported by Pratt and Whitney Aircraft, Commercial Products Division.

References

1 Langston, L. S., Nice, M. L., and Hooper, R. M., "Three-Dimensional Flow Within a Turbine Cascade Passage," ASME JOURNAL OF ENGINEERING FOR POWER, Vol. 99, Jan. 1977, pp. 21–28.

2 Herzig, H. Z., Hansen, A. G., and Costello, G. R., "A Visualization Study of Secondary Flows in Cascades," NACA Report 1163, 1953.

3 Horlock, J. H., "Cross Flows in Bounded Three-Dimensional Turbulent Boundary Layers," *Journal of Mechanical Engineering Science,* Vol. 15, No. 4, 1973, pp. 274–284.

4 Johnston, J. P., "On the Three-Dimensional Turbulent Boundary Layer Generated by Secondary Flow," ASME *Journal of Basic Engineering,* Vol. 82, 1960, pp. 233–248.

5 Nash, J. F. and Patel, V. C., *Three-Dimensional Turbulent Boundary Layers,* SBC Technical Books, Atlanta, 1972.

6 Klinksiek, W. F. and Pierce, F. J., "Simultaneous Lateral Skewing in a Three-Dimensional Turbulent Layer Flow," ASME *Journal of Basic Engineering,* Vol. 92, 1970, pp. 83–92.

7 Shanebrook, J. R., "An Approximate Method of Treating the Three-Dimensional Incompressible Boundary Layer Equations when Crossflow is Small," Ph.D. Thesis, Syracuse University, Sept. 1965.

8 Eichelbrenner, E. A., "Theoretical Investigation and Control by Measuring Tests on the Behavior of the Three-Dimensional Turbulent Boundary

Layer on an Annular Wing at Various Incidences," Bureau Technique Zborowski, Brunoy, 1963.

9 Johnston, J. P., "Experimental Studies in Three-Dimensional Turbulent Boundary Layers," Report MD-34, Dept. of Mechanical Engineering, Stanford University, July 1976.

10 Wheeler, A. J., and Johnston, J. P., "An Assessment of Three-Dimensional Turbulent Boundary Layer Prediction Methods," ASME *Journal of Fluids Engineering,* Sept. 1973, pp. 415–421.

11 Pratap, V. S., and Spalding, D. B., "Fluid Flow and Heat Transfer in Three-Dimensional Duct Flows," *International Journal of Heat and Mass Transfer, 19,* 1976, pp. 1183–1188.

12 Briley, W. R., and McDonald, H., "Computation of Three-Dimensional Subsonic Flow in Curved Passages," United Aircraft Research Laboratory Report R75-911596-8, 1975.

13 Dodge, P. R., "A Numerical Method for Two and Three-Dimensional Viscous Flows," AIAA Paper No. 76-425, AIAA 9th Plasma and Fluid Dynamics Conf., San Diego, CA, 1976.

14 Ghia, K. N., Ghia, V., and Studerus, C. J., "Analytical Formulation of Three-Dimensional Laminar Viscous Flow through Turbine Cascades using Surface Oriented Coordinates," ASME Paper No. 76-EE-22, 1976.

15 Waterman, W. F., and Tall, W. A., "Measurement and Prediction of 3-D Viscous Flows in Low-Aspect-Ratio Turbine Nozzle," ASME Paper No. 76-GT-73, 1976.

16 Sjolander, S. A., "The Endwall Boundary Layer in an Annular Cascade of Turbine Nozzle Guide Vanes," Tech. Report No. ME/A 75-4, Dept. Mech./Aero. Engr., Carleton University, Ottawa, Canada, Dec. 1975.

17 Carrick, H. B., "Secondary Flow and Losses in Turbine Cascades with Inlet Skew," Ph.D. Thesis, Cambridge University, Oct. 1975.

18 Marchal, Ph., and Sieverding, C. H., "Secondary Flow within Turbine Bladings," AGARD-CPP-214 (Netherlands), *Secondary Flow in Turbomachines,* Mar. 1977.

19 Dring, R. P., "A Momentum-Integral Analysis of the Three-Dimensional Turbine Endwall Boundary Layer," ASME JOURNAL OF ENGINEERING FOR POWER, Vol. 93, Oct. 1971, pp. 386–396.

20 Booth, T. C., "An Analysis of the Turbine Endwall Boundary Layer and Aerodynamic Losses," ASME Paper No. 75-GT-23, Mar. 1975.

21 Barber, T. J., and Langston, L. S., "Three Dimensional Modelling of Cascade Flows," 79-0047 AIAA, Jan. 1979.

22 Stanitz, J. D., Osborn, W. M., and Mizisin, J., "An Experimental Investigation of Secondary Flow in an Accelerating, Rectangular Elbow with 90° of Turning," NACA TN 3015, 1953.

23 Mellor, G. L., and Wood, G. M., "An Axial Compressor End-Wall Boundary Layer Theory," ASME *Journal of Basic Engineering,* June 1971, pp. 300–316.